High-Resolution LES of a Starting Jet

E. Inanc[a,*], M. T. Nguyen[a], S. Kaiser[b], A. M. Kempf[a]

[a] *Chair of Fluid Dynamics*
[b] *Chair of Reactive Fluids*
Institute for Combustion and Gasdynamics, Universität Duisburg-Essen, Germany

Abstract

An impulsively started jet is investigated by a highly resolved large-eddy simulation (LES). The numerical calculations are presented, analyzed and compared to the experimental data by Soulopoulos et al. (2014). Different inlet velocity profiles and their turbulence intensity are employed in the simulations to identify the appropriate boundary conditions by comparing the obtained mixture fraction and its dissipation rate against the experimental data. A sensitivity analysis of the numerical calculations to the different filter sizes is performed, and the ramp-up functions of the inlet flow are investigated. A satisfactory agreement between the simulation and the experiment is achieved. It is found that the potential core, which is observed in our calculations, was absent in the experiments, likely due to premature mixing in the nozzle.

Two parameters, namely the mixture fraction and its dissipation rate, are chosen for the statistical evaluation, which is presented for both the calculation and the experiment. It is clear that the initial/boundary conditions influence the flow dynamics, thus considerable differences in the statistics can be observed. The comparison of the resolved scales shows that the simulation resolves structures smaller than those from the experiment by a factor of two. However, this does not lead to the discrepancy of the numerical and experimental statistics, which is independent of the resolution. It is observed that the high scalar dissipation rate (SDR) values are mainly located in the mixing layer, however the vortex ring is occupied by the considerably lower SDR values.

Keywords: Large eddy simulation, Starting jets, Pulsed jets, Vortex ring, Scalar mixing, Scalar dissipation rate.

1. Introduction

Starting jets play a fundamental role in engineering applications such as injectors, pulsed-jet propulsion and mixers, but also in physiological flows. The physical behavior of these types of jets is commonly observed in petrol and Diesel direct injection engines, where pulsed injections are applied to exploit the rapid mixing. The initial burst of a jet from an orifice tears the environment, forms a vortex ring and evolves into a high-momentum axisymmetric column structure. Consequently, the entrained air in the vortex ring slows this axisymmetric structure down due to the low momentum added to the jet. When this vortex ring is filled with the maximum momentum it can absorb, it pinches off from the main jet, which usually happens at a short distance downstream of the nozzle. The entrained air in the detached vortex ring diffuses rapidly resulting in enhanced mixing. Most studies on starting jets [1, 2, 3, 4] focus on the early jet phases, whereas the subsequent evolution of the jet after the pinch off has seen less interest so far [5].

A key topic of these studies is the evolution of the vortex ring [6, 7, 8]. Witze [9, 10] used a hot-film anemometer to derive equations for determining the velocity, size and location of the vortex ring. It was found that the jet penetration scales linearly with time for the early phases until the tip of the jet reaches seven nozzle diameters; later on the penetration length scales with the square root of time [11]. It was shown that the transient jets are similar depending on the characteristic-time similarity parameter, which is defined as the ratio of the nozzle diameter to the injection velocity.

A starting jet has a considerable physical differences compared to a quasi-steady jet. The tip velocity of a starting jet is approximately one-half of the center-line velocity of the steady jet variant [12, 13], and the growth of the width of a starting jet is proportional to the distance traveled [4]. The entrainment rate of starting jets is nearly twice that of the steady jets [14], and the mixing at the tip of the jet is enhanced as the jet travels further downstream [12, 13]. The starting jet's physical characteristics show great similarity to the quasi-steady jets between the nozzle and the vortex ring [15].

Simulations of starting jets can provide more information about the evolution of the vortex ring than most experiments, as illustrated in the works of Nitsche and Krasny [16] or Heeg and Riley [17]. Janicka and Kollmann [18] predicted the centerline velocity decay and spreading rate of a jet using a simple turbulence model. Rosenfeld et al. [19] and Zhao et al. [20] showed that the maximum circulation of the vortex rings heavily depends on the velocity profile at the nozzle exit and the perturbations of the upstream flow. Impinging starting jets are of particular interest [21] since they are relevant for fuel injection in IC engines.

The mixing processes in starting jets are of considerable interest for reactive cases [22, 23, 24, 25]; Kato et al. [26] showed that a starting jet has a higher mixing rate than the steady jets due to the additional mixing in the vortex core. Takagi et al. [1] observed high spatial gradients in the vortex core and the mixing

*Corresponding author, Tel: +49 203 3798133, Fax: +49 203 3798102, Address: Universität Duisburg-Essen, Faculty of Engineering, Chair of Fluid Dynamics, Carl-Benz-Str. 199, D-47057, Duisburg/Germany.
Email address: eray.inanc@uni-due.de (E. Inanc)

layer, which are essential for combustion. Southerland et al. [27] pointed out that the mixing in the vortex core is limited to the air entrained during the formation of the vortex ring. It was also found that the entrainment rate of the jet is greatly affected by the frequency of the injection in the impulsively started jets [28, 29, 30].

The enhanced mixing achieved by the nature of these jets is commonly exploited in non-premixed combustion, where the chemical reaction occurs after fuel and oxidiser are mixed at a molecular level. Transient mixing stirs the reactants at large scales and enhances the mixing by increasing the scalar gradients. Since molecular mixing occurs on the smallest scales by diminishing the scalar gradients, the scalar dissipation rate (SDR) is of fundamental interest in the turbulent mixing of two media [31, 32, 33] and hence for non-premixed combustion. The SDR is defined by $\chi = 2D_\phi(\partial\phi/\partial x_i)(\partial\phi/\partial x_i)$, where D_ϕ is the scalar diffusivity. Many measurements have been performed to investigate the scalar mixing and SDR involving various flow visualization techniques [23, 34, 35, 36, 37, 38, 39, 40, 41, 42] in 0-3D measurements. The statistical analysis of the SDR in a turbulent flow showed that the SDR's probability density function (PDF) has a log-normal behavior [43, 44].

Soulopoulos et al. [45] recently measured the SDR of an impulsively started gas jet using planar laser induced fluorescence (PLIF), where a log-normal PDF of the SDR was observed in their experimental statistics as well [46]. Their experiment injected air with an acetone tracer into ambient air, providing excellent optical access.

Different length scale requirements for resolving these small-scale quantities, such as the SDR, are estimated using energy and dissipation spectra by Wang et al. [47]. When calculating the SDR, it is clear that the spatial resolution of the measurements and simulations should be in the Kolmogorov or Batchelor length scale ranges. The simulations performed to estimate the SDR are challenging, since resolving Kolmogorov or Batchelor scales requires very fine computational grids. The SDR is preferably investigated by large eddy simulation (LES), which reduces the computational effort compared to DNS. However, this approach highly depends on the sub-grid models for resolving sub-grid contributions to the SDR.

A recent study by Dunstan et al. [48] analyzed the statistical behavior of the SDR in the context of DNS and LES of turbulent premixed combustion using simplified chemistry for a turbulent V-flame. Ma et al. [49] tested a SDR-based combustion model for the LES of turbulent premixed flames. Pitsch and Steiner [50] have investigated scalar mixing and the SDR in Sandia Flame D [51] with complex physics using LES, before others looked into further detail [52]. Recently, Wang et al. [53] performed measurements for a transient turbulent jet flame, where an LES was performed as well to provide a new benchmark for studying the effects of turbulence-chemistry interaction.

Many different statistical approaches for the conditional SDR in turbulent flows have also been tested to model the SDR [54, 55]. Since the rate of mixing limits the chemical conversion process in non-premixed combustion, the SDR is a key parameter for many turbulent combustion models [56, 57, 58, 59, 60], often

based on Peters' works on flamelet modelling [59], where non-premixed [52, 61] and premixed [62, 63] combustion are modeled using SDR as the source term.

This paper presents a detailed numerical investigation for the mixing process in an impulsively starting jet, which has been absent in the literature to our best knowledge. The structure of this paper is as follows: The experimental setup and numerical models are given in Section 2 and Section 3, respectively. In Section 4, our simulation is validated with the experiment, where the major differences are discussed. Followingly, the parameters that are unknown from the experiments, but affected the numerical results, are investigated. Finally, the statistical investigation of the mixing is presented.

2. Experiment

2.1. Flow configuration

This work numerically reproduces the experiment performed by Soulopoulos et al. [45]. The measurement was carried out on a high-velocity jet flow of air (u_{jet} = 20 ms^{-1}) with acetone tracer emanating into a homogeneous low-velocity co-flow ($u_{\text{co-flow}}$ = 0.1 ms^{-1}). A commercial automotive gas injector (Keihin-KN3-2B) was used; the valve was placed 20 mm upstream of the nozzle exit in a straight tube with a nozzle diameter of D = 4 mm. The experimental set-up is illustrated in Fig. 1. Throughout the measurements, the pressure of 1 bar and the temperature of 65°C were kept constant. The solenoid valve's opening time t_v was estimated to be less than 1 ms. The Reynolds number at the nozzle was about 4500 during the steady flow phase, assuming a kinematic viscosity of $\nu = 1.75 \cdot 10^{-5}$ m^{2}s^{-1}.

The characteristic-time similarity parameter [10] $\tau = D/u_{jet}$ is estimated as 0.2 ms, where D is the diameter of the nozzle. This parameter is used to define a non-dimensional time. Consecutive injections occurred every 500 ms, which was selected in order to avoid the interaction between the two pulses; each injection lasted 10 ms.

The jet was injected into a cubic chamber of the dimensions of 300 mm x 300 mm x 300 mm. The bottom of the chamber has both the co-flow inlet and the nozzle; the upper part was open to the atmosphere. The co-flow air generated a homogeneous flow field inside the chamber. The inlet velocity profile, the exact valve opening duration, the initial ramp-up (ramp-down) duration and the lip thickness of the nozzle are not known from the experiments, therefore the effects of these unknown initial/boundary conditions on the flow dynamics had to be investigated (Section 4.2).

2.2. Measurements

Soulopoulos et al. [45] took a PLIF measurement every fourth injection. A laser beam at 266 nm with a Gaussian characteristic excited the acetone to fluoresce; three cylindrical lenses formed a laser sheet, 45 mm high and 130 µm thick. A CCD camera recorded the emission. A total of 300 samples was obtained.

The measured data were post-processed at each start of an injection (SoI) time of 1.93 ms. With constant temperature, constant pressure and at the optically thin limit, the fluorescence intensity was proportional to the laser beam energy and the acetone concentration, which allowed conversion into a mixture fraction field after calibration across the field of view.

The image noise was reduced by a Wiener filter. From the filtering errors, the accuracy of the mixture fraction and SDR were estimated to be approximately 98% and 80%, respectively. The numerical errors in the calculation procedure of the gradients were corrected based on the work by Tanaka and Eaton [64]. Because of the optical methods used, only two-components, radial and axial gradients, were available to calculate SDR. The in-plane components $\partial f/\partial x$ and $\partial f/\partial y$ of the scalar gradient vector ∇f, were computed using central differences around each grid point in the PLIF data plane. We employed the same SDR calculation method in our results for meaningful comparison.

The pixel spacing and the spatial resolution of the experiment were given as 45 µm/pixel (for the 1024 x 1024 pixels^2 CCD array) and 250 µm (according to the DPS), respectively. The Kolmogorov length scale was estimated around 4.4 µm ($\eta_K = \nu^{0.75}/\epsilon^{0.25}$ [65]), hence the calculated Batchelor length scale was 5.3 µm ($\eta_B = \eta_\kappa \cdot Sc^{-0.5}$ [66]), the laminar and turbulent Schmidt numbers were taken as $Sc = 0.7$. The smallest scalar scales observed in the experiment and the simulation were also estimated from the dissipation power spectrum (DPS) following the method of Wang et al. [47].

3. Numerical modelling and set-up

This work employs Bilger's definition of the mixture fraction [67], which is transported via Eq. (1).

$$\frac{\partial}{\partial t}(\overline{\rho}\tilde{f}) + \frac{\partial}{\partial x_i}(\overline{\rho}\tilde{f}\tilde{u}_i) = \frac{\partial}{\partial x_i}\left(\overline{\rho}\widetilde{D}_f\frac{\partial \tilde{f}}{\partial x_i} + \overline{\rho}F_i^R\right) \tag{1}$$

In Equation (1), the term F_i^R represents the non-resolved scale contribution of mixture fraction flux, which is estimated according to the eddy diffusivity approach [68], modelled as in Eq. (2). The factor $\widetilde{D_f}$ is the laminar diffusion coefficient. A constant density $\overline{\rho}$ is assumed in this work.

$$F_i^R = D_{f,t}\frac{\partial \tilde{f}}{\partial x_i} \tag{2}$$

The turbulent diffusivity is estimated from the turbulent viscosity as $D_{f,t} = \nu_t/Sc$. The turbulent viscosity ν_t is calculated by the Smagorinsky model [69] with a fixed model constant of $C_m = 0.173$ [70] to avoid the effect of an additional variable on the parameter studies (the model by Nicoud et al. [71], and different model constants were tested, however the difference was negligible).

Case	Domain [mm]	Cells [Mio.]	Δ [η_K]	ℓ_t [mm]	CPUs	Time [CPUh]	Run-time [ms]	$(\nu_t/\nu)_{max}$
C-1/1	300×300^2	27	227.3	1.0	16	80	3	16.2
C-2/3	200×200^2	64	68.2	1.0	96	960	3	4.86
C-1/2	150×150^2	422	45.5	1.0	144	3,500	3	2.73
C-1/4	75×75^2	422	22.7	1.0	144	7,000	3	1.65
C-1/6	50×50^2	374	15.9	0.5	144	5,800	3	1.22
C-1/10	**40×30^2**	**563**	**9.10**	**0.5**	**192**	**18,500**	**3**	**0.53**
C-1/10-M	40×30^2	71	18.2	0.5	144	2,000	3	1.30
C-1/10-C	40×30^2	9	36.4	0.5	144	35,000	*15,000*	2.72

Table 1: Properties of the investigated cases. The filter (cell) size Δ is given relative to the Kolmogorov scale ($\eta_K = 4.4$ µm). The finest simulation is highlighted.

The sum of the resolved and the un-resolved part of the SDR is modelled with a simplified variant of the model proposed by Girimaji and Zhou [72], which was successfully employed before [52, 73]. Hence, the SDR is rewritten as in Eq. (3).

$$\widetilde{\chi} = 2(\widetilde{D}_f + D_{f,t}) \frac{\partial \widetilde{f}}{\partial x_i} \frac{\partial \widetilde{f}}{\partial x_i} \tag{3}$$

The simulations are performed using the LES in-house solver PsiPhi [49, 74, 75, 76, 77, 78]. This code solves the filtered Navier-Stokes equations on equidistant Cartesian grids by the finite volume method. The convective fluxes of the momentum are discretized by 2$^{\text{nd}}$ order accurate central differencing, scalar convection is discretized by a total variation diminishing scheme with the *CHARM* limiter function [79]. Time integration is performed by the 3$^{\text{rd}}$ order accurate low-storage Runge-Kutta scheme [80], where the time step width Δt is determined by the CFL condition [81] for a constant value of 0.7. The domain is uniformly decomposed into sub-domains assigned to different cores; the Message Passing Interface (MPI) is used for communication between these sub-domains.

Inlet boundary conditions are specified on the nozzle exit plane ($x = 0$, Fig. 1). The velocity profile at the nozzle exit is derived from the 7$^{\text{th}}$ power law turbulent velocity profile described in [82], and several different velocity profile alternatives are compared. The jet velocity is ramped up linearly in 250 μs (Fig. 9a, *Ramp a*). At the end of the pulse, the jet is linearly ramped down over 250 μs.

Artificial turbulence, with an intensity of 5% is generated at the inlet using the method suggested by Klein [83, 84]. The effects of the turbulence intensity are analyzed in Section 4.2. Two different turbulent length scales (1 mm and 0.5 mm) were tested, but no considerable effects were observed. Table 1 gives the different cases regarding domain sizes, grid sizes and computational resources. The cases are named by the scaling of the experimental domain to the computational domain. For example 'C $-$ 2/3' means that the dimensions of the computational domain are reduced two-thirds in each direction with respect to the experimental domain, which yields an approximately three times smaller control volume. The letters 'M'

and 'C' denote medium and coarse simulations, respectively.

4. Results

4.1. Qualitative comparison of results.

We represent the development phase of the starting jet (Fig. 2) by showing the axial velocity (Figs. 2a-d), the mixture fraction (Figs. 2e-h) and the corresponding SDR (Figs. 2i-l) at different times [3.3τ, 5.7τ, 8.1τ, 10.3τ].

In Figures 2a-d, the velocity contours show that the highest axial velocities are found at the lead vortex ring near the potential core. The vortex ring causes a strong back-flow at its outer edge. Figures 2c-d show that the axial velocity decreases at the axial distance of $x/D = 2 - 3$, which should be the location where the jet will pinch-off.

The estimated mean jet tip velocities from Figs. 2a-d are [6.96, 8.45, 9.78, 9.47] ms^{-1}, respectively. Apart from the recorded velocity for the early jet, these velocities are approximately one-half of u_{jet}, similar to the findings by Johari et al. [12, 13]. The penetration length is defined by the axial position of the most downstream point with $\tilde{f} > 0.1$.

It can be observed from Figs. 2e-h that the mixing layer thickness increases, and gets more wrinkled over time. The mixing layer far downstream is also considerably thicker than near the inlet. From Figs. 2i-l, it can be seen that high SDRs are initially located at the outer mixing layer (Fig. 2i). In later phases, high SDRs are also visible at the vortex core (Fig. 2l) due to the entrainment of some air.

In Figure 3, the calculated normalized jet penetration length over the square root of non-dimensional time for case C-1/10-C is compared to the theoretical one from the work of Witze [9], where a dyed liquid jet is injected into a container filled with water. Related work was done by Cossali et al. [85], the latter for gas jets, showing similar results.

As seen in Fig. 3, the predicted jet penetrates the domain linearly with time until $x/D \approx 7$ (or $t/\tau \approx 3.35$), and with the square root of time afterwards. This matches very well with the fitted theoretical findings [10, 11]. The jet diffuses completely over time from the valve shut down at 50τ.

The mean velocity at the tip of the jet is also recorded (Fig. 3), and compared to the fitted theoretical expression [11]. Apart from the initial ramp-up of the starting jet, the calculated tip velocity agrees well with the analytically calculated velocity. Later on, the tip velocity degrades rapidly due to dissipation. This behavior matches to the analytical solution.

The expansion angle of the jet, which is the angle between the maximum radial distance of the jet to the location of the nozzle edge at the inlet, is estimated to be approximately 10°, which is in agreement with the experiments [9, 10, 11, 45].

The computed instantaneous mixture fraction and the SDR fields are compared against the experimental data [45] in Figs. 4 and 5. The mixture fraction distributions from the simulation (Fig. 4a) and the experiment (Fig. 4c) show however a poor agreement mainly because of the potential core observed in the simulations. Apparently, the small scale structures in the mixing layers are better resolved in the simulation (Fig. 4a) than the experiment (Fig. 4c), where the grid size for the simulation is 40 µm compared to 250 µm for the experiment.

To enable a comparison of the simulations with the experiment, the simulation plots were post-processed (Fig. 4b): The raw mixture fraction field was rescaled to the highest mixture fraction value observed in the experiment, and a low-pass filter (Gaussian, $\sigma = 0.125\Delta^{-1}$) was applied after adding some Gaussian noise (1% variance) to represent the effect of the unsharpness and the noise in the optical diagnostics. This process yields similar mixing layer shapes of the jets, but experiments (Fig. 4c) imply that the mixture fraction values decrease from the inlet. This behaviour was not expected, since the potential core is clearly observable at similar cases [12, 13, 29, 30, 22, 23, 86, 87].

Soulopoulos et al. [88] explain the lack of a potential core with the ambient air being entrained into the nozzle between the successive injections, leading to a premature mixing between the inflow and the co-flow inside the nozzle prior to the injection. Assuming that Soulopoulos' explanation for the missing potential core is correct, we post-processed the experiment to make the mixture fraction fields more comparable (Fig. 4d). The data was rescaled in each y-z plane in such way that the maximum mixture fraction value there is 1; the result resembles a jet with a potential core. The reconstructed potential core (dark-red color in Fig. 4a) achieves qualitative agreement with the simulation (Fig. 4d) up to an axial distance of $x/D = 3$. This implies that Soulopoulos' explanation of pre-injection mixing is likely to be correct.

Another difference between the experiment and the simulation is the thicknesses of the mixing layers. We assume that a possible cause is the laser beam profile and a relatively thick laser sheet in the experiments, whose influence on similar experimental data are discussed by Kaiser and Frank [89]. Near the inlet, we can estimate the diffusion layer thickness as $l_D = \sqrt{D_f \; t_D}$, where $t_D = L/u_l$ is the characteristic diffusion time, and L is the downstream distance. Assuming a velocity scale u_l of half of the jet exit velocity (10 ms^{-1}), this yields a 0.1 mm thick mixing layer at $x/D = 1$, which is in good agreement with the thickness observed in the simulation (Fig. 4a) at the same location.

The experiment (Fig. 4c) shows a thicker mixing layer, which is clearly observed near the nozzle, compared to the analytical solution and the simulation data. According to Soulopoulos et al. [45], the optical setup and the numerical error correction filters that are used to reconstruct the mixture fraction signal cause some broadening, or expansion of the mixture fraction profile.

As can be seen in Fig. 5a, high SDR is observed in the mixing layer and the transition layer, which is the layer between the vortex ring and the potential core. The rescaling and filtering yields Fig. 5b, where the diffusion layer thickness increases to about 0.3 mm, which is very similar to the experimental thickness

	Study 1	Study 2	Study 3	Study 4
Test cases	* 5	C-1/10-C	C-1/10	C-1/10-M
Ramp duration, t_a	0.25 ms	0.25 ms	0.25 ms	* 2
Velocity profile	top hat	average	* 4	top hat

Table 2: Parameter studies presented in Section 4.2, the varied parameters are indicated by an asterisk, the different number of cases considered are by the trailing number.

in Fig. 5c. The post-processed experimental SDR (Fig. 5d) shows SDR values 'agreeing' better with the simulations, however the difference is still considerable.

Figure 6 presents the vorticity field calculated from axial and radial velocity components. The vorticity reveals the approximate location of the vortex ring. As expected, the vorticity at the vortex rings increases over time, where at the initial state (Fig. 6a) the fluid is bursting out of the inlet in axial direction only. At later times (Fig. 6d), the vorticity increases both in the vortex ring and in the mixing layer.

4.2. Effect of physical and modelling parameters on results

The effects of the grid size on the numerical results are investigated by comparing mixture fraction fields as presented in Fig. 7. The configuration of the test cases is given in Table 2, *Study 1*.

It can be seen that the jet break-up is delayed for very coarse meshes (Figs. 7a-c), where a good qualitative agreement with the experiment is achieved for the medium and fine meshes (Fig. 7d). Furthermore, the predicted physical structures of the jet of the medium case (Fig. 7d) look very similar to those from the fine case (Fig. 7e) despite it's lower resolution.

The jets with different grid sizes have almost the same plume area, where the details of the mixing layer and the amount of entrained air in the vortex core are slightly different. It is observed that the coarser cases (Fig. 7a-b) have preserved their axisymmetric column structure. In the cases with higher resolution (Fig. 7c-e), the mixing layer is deformed due to more resolved turbulence, and is thicker than those obtained from the coarser cases (Fig. 7a-b) (It should be noted that this comparison would ideally be conducted by multi-injection simulations, which was not possible in this work due to the cost involved for the finest simulation).

According to the experimentalists [45], the flow remains inhomogeneous between the consecutive injections. To study the flow field, a sequence of injections was simulated. To avoid excessive simulation costs, a relatively coarse grid was selected for this study. Different realizations of instantaneous mixture fraction fields, with parameters given in Table 2, *Study 2* are presented in Fig. 8. It is observed that the penetration length minimally differs for each realisation, and that the jets from different realisations are highly reproducible.

The inlet velocity profile in the experiment is not known. To study the impact of the inlet velocity profile on the mixture fraction field, simulations with different velocity profiles are compared to each other. The

tested inlet velocity profiles (Gaussian, top-hat, 7^{th} power-law and averaged velocity profiles) are visualized in Fig. 9a. The Gaussian velocity profile has a standard deviation of $\sigma = 0.25D$. All profiles have the same mass flow as the experiment. The 'average' profile obtained from the average between the top-hat and the power law profiles is supposed to model a semi-developed turbulent velocity profile.

The results are presented in Fig. 10, the simulation parameters are given in Table 2, *Study 3*. Given the short length of the nozzle downstream of the valve and the pulsed nature of the jet, we may assume that the velocity profile is 'a mix' of a top-hat plug flow and a fully developed pipe flow. The 'average' inflow profile is meant to test this assumption (Fig. 10d).

The jet using the Gaussian velocity profile in Fig. 10b is narrower and longer than the one from the top-hat profile (Fig. 10a), whereas the jet with the 7^{th} power law profile (Fig. 10c) penetrates deepest. The penetration length for the 'average' profile agrees best with the experiment. The jets with top-hat and Gaussian profiles have more smooth edges than the jets with the 7^{th} power law and the 'average' profiles. The possible argument is that the pinch off location of the lead vortex depends on the inlet velocity profile [19], where different pinch off locations may yield wider mixing/diffusion layers at the edge of the jet, especially at the top part.

In the simulations, we found that the ramp-up duration of the flow at each SoI has a strong influence on the flow field, but the real ramp-up profile from the experiment is not known. Two different ramp up functions, shown in Fig. 9b as *'sudden'* and *Ramp-b* were therefore compared, where the total injected mass was kept constant in Fig. 11 (This comparison does not include the *Ramp-a* function as it's behavior hardly deviated from that of the *'sudden'* jump).

Due to the more slowly accelerated jet flow, the penetration length in Fig. 11b is shorter than that of the sudden ramp-up variant (Fig. 11a) by 5 mm. The jet in Fig. 11b shows that the vortex ring is still intact, where it is clear that the magnitude of the acceleration is directly linked to the vortex ring dynamics.

The influence of the turbulence intensity at the inlet on the mixture fraction field is also investigated. The mixture fraction plot, where the turbulence intensity is linearly increased by Ramp-b function (Fig. 11c), shows that the initial turbulence affects the top region of the jet the most. We observe that the ramped turbulence intensity prevents the formation of a vortex ring, and that the mixing layer is influenced as well.

As the experiment does not show a clear potential core, one may raise a question if the mixture fraction should also be ramped up smoothly to better represent the premixing in the nozzle. We investigated this phenomenon by ramping up the mixture fraction at the nozzle linearly from 0.4 to 1 over 2 ms (Fig. 11d), where the tip of the jet is affected.

Finally, we tested how a combined ramp-up of these parameters would affect the results (Fig. 11e). The linear acceleration of these parameters yields completely different jet dynamics, with the jet much wider than that shown in Fig. 11a (around 2-3 mm) and a clear vortex ring is not formed. Similar penetration lengths are observed in Figs. 11b and e. It is plausible that the ramping-up of the turbulence intensity may

not influence the jet characteristics for the jets with slowly ramped-up inlet velocities.

To conclude, we observe that the parameters inlet velocity $\tilde{u}$, the turbulence intensity I and the mixture fraction $\tilde{f}$ affect the flow field and mixing. Future experiments should make an effort to quantify them at the inlet as a function of time. For the present case, the closest agreement with the experiments was achieved with a *linear* ramp-up (ramp-down) with a duration of *250 μs*, a *semi-developed turbulent velocity profile* (averaged from top-hat and 7^{th} power law profiles), a turbulent length scale of *0.5 mm* and a turbulence intensity of *5%*.

4.3. Statistical evaluation of results

This section compares the averaged mixture fraction and SDR from the simulations against the experimental values. For the finest case (C-1/10), only four samples from a single injection along different radial planes were affordable, but for the less costly case C-1/10-C, a total of 32 injections were used to obtain 32 samples.

We can observe in Fig. 12 that the plot from four samples (Fig. 12b) has a greater similarity to the mixing layer of the instantaneous images from the experiments (Fig. 4d) than the two sample variant (Fig. 12a). Filtering the averaged simulation data increases the similarity of this mixing layer relative to the experimental one. It should however be noted that in the averaged experimental plot (Fig. 12d), the vortex ring is hardly visible.

The averaged mixture fraction plot over 32 samples from the coarse case C-1/10-C (Fig. 12c) shows a 3 mm deeper penetration length. A very smooth mixing layer is observed, which is similar to the averaged experimental data (Fig. 12d). However, in every averaged simulation (Figs. 12a-c), a potential core is present, which is not observable in the averaged experiment (Fig. 12d), as discussed in Section 4.1. Furthermore, the expansion angle in the simulations (10°) is in reasonable agreement with the experiment (11°).

The root mean square (RMS) of the mixture fraction is shown in Fig. 13b. We observe that the high deviation of the mixture fraction is mainly located at the top region of the jet.

The SDR fields for all cases (Figs. 12e-h) display a visible layer of high SDR around the jet, whereas the peak values, as seen in similar cases [39, 44], are located near the inlet and in the region of high compressive strain at the tip of the jet. A comparison of the simulation and the experiment is shown in Figs. 12g and 12h.

The radial profiles of the mixture fraction at four axial locations ($x/D = 1, 2, 3, 4$) at the time 9.65τ are presented in Fig. 14. The simulation data are rescaled as described in Section 4.1. Figure 14b indicates that the average jet profile shows reasonable agreement with the measured data. The calculated radial profile near the nozzle agrees with the experiment, but the width of the simulated jet at $x/D = 2 - 3$ is narrower

	Plume Area	Plume Volume
Simulation	$A_s \approx 126$ [mm^2]	$V_s \approx 687$ [mm^3]
Experiment	$A_e \approx 156$ [mm^2]	$V_e \approx 985$ [mm^3]
Difference	14%	31%

Table 3: Estimated plume area and plume volume from the averaged simulation data over 4 samples of C-1/10 compared with instantaneous experimental data.

than that from the experiment, but similar at $x/D = 4$. Figure 14c shows three consecutive injections in a simulation, where we observe insignificant differences.

In a further attempt to compare the simulation and the experiment, we examine the plume area A and plume volume V, which are computed from the four sample averaged data (C-1/10) and the experimental data via Eqs. (4). In these equations, the central-plane surface is $S(x, y)$. The stored mixture fraction value at each grid point in the domain is represented as $f(x, y)$. The term $r = \sqrt{x^2 + z^2}$ denotes the distance of a grid point to the centreline of the domain, the arrow ' $\rightarrow$ ' means that the $f(x, y)$ is set to 1 for mixture fractions $\tilde{f}$ greater than 0.05. Table 3 shows the results obtained.

Overall, the difference in the plume area and volume between the experiment and simulation remain considerable. As described earlier (Fig. 14a), this can be observed at axial distances $2 < x/D < 3$, where the simulated jet is narrower than the experimental jet.

$$
\begin{aligned}
A &= \Delta^2 \int_S (f(x,y)|_{>0.05} \rightarrow 1)\ dS \\
V &= \Delta \int_S \pi r^2 \cdot (f(x,y)|_{>0.05} \rightarrow 1)\ dS
\end{aligned}
\tag{4}
$$

The PDFs of the normalized conditional logarithm of the SDR are shown in Fig. 15, where the SDR is calculated from the two-gradient ($\partial f/\partial x$, $\partial f/\partial y$) and three-gradient ($\partial f/\partial x$, $\partial f/\partial y$, $\partial f/\partial z$) components of the experimental and numerical mixture fraction fields, respectively. The PDFs are normalised using the local mean μ and standard deviation σ values of $\ln(\tilde{\chi})$, and the SDR are conditioned on the mixture fraction with values higher than 0.05.

In Figure 15, the PDFs agree with the expected log-normal distribution (Gaussian), as reported in the Literature [39, 43, 46, 90, 91]. It is clearly seen that the different resolutions (Fig. 15c), the calculated SDR from two or three dimensional gradients (Fig. 15d) and different viscosities (Fig. 15e) hardly change the shape of the PDFs. Similar PDFs are observed for different realizations (Fig. 15b).

Figure 16 shows the averaged conditional distribution of SDR over the mixture fraction. Clearly, the overall SDR values are smaller in the experiments by a factor of ten, which is likely due to the lower resolution and the absence of the potential core. Figure 16a shows that the SDR decreases over time, mostly in the mixture fraction range of 0.6-0.8, which occurs in the vortex ring during its initial formation.

The grid dependency of the conditional averages of SDR is investigated in Fig. 16b, which shows that a finer grid yields higher mixture fraction gradients. Furthermore, the curves of the conditional distribution calculated from the simulations with coarser grid sizes (C-1/10-C and C-1/10-M in Fig. 16b) show some similarity to the fine one (C-1/10), such as the SDR decay at similar mixture fraction ranges. Since the finest simulation (C-1/10) is still not a DNS, the contribution of the SGS model to the SDR is noticeable mostly in the mixture fraction region of 0.6-0.8 (Fig. 16c), where these values occur mostly in the vortex ring, however the SGS model contribution to the SDR is negligible.

Figure 17 presents the instantaneous conditional distribution of SDR over the mixture fraction for both the experiment and the simulation. The colors indicate the axial location of each data point. The experiments show high SDR in the mixture fraction range of 0.6-1 only near the inlet (Fig. 17a). Compared to the simulations, the high SDR in the experiment are shifted downstream. According to Fig. 17b, the lowest SDR values are found in the vortex ring. However, this is not clearly appearing in the experimental scatter plot (Fig. 17a).

The cluster of low SDR values shifts from high mixture fraction (0.6-0.8) to lower ones (0.5-0.7), and the SDR values further decrease as observed in Figs. 17a-b. This is due to the mixing in the vortex core, which is only limited to the entrained air during the initial vortex formation. This mixing process is rapidly completed in early jet phases, and since there is no more mixing the SDR values become very low.

Dissipation power spectra (DPS) for both simulation and experiment are presented in Fig. 18. The smallest resolved scale is estimated by the method of Wang et al. [47] for both the experiment and the simulation. For C-1/10 (Fig. 18a), we estimate a smallest resolved scalar scale in axial direction of $40.9\eta_\kappa$ (0.18 mm) and in the radial and circumferential directions of both $49.9\eta_\kappa$ (0.22 mm). At the same time and location, the experiment yields a smallest resolved scalar scale of $72.5\eta_\kappa$ (0.32 mm), which is two times larger than in the simulation. The grid size used in C-1/10 (0.04 mm) is finer than the smallest resolved scalar scale by a factor of 4.5, which is observed for different grid sizes (C-1/10-C and C-1/10M in Fig. 18b). It should be noted that the physical Batchelor scale is still smaller, typically of the order of the Kolmogorov scales.

In LES, the added artificial turbulence by numerical models determines the quality of the simulation, which could be approximated by the ratio of the turbulent to the laminar viscosities ν_t/ν.

Figure 19 shows the calculated viscosity ratios for cases C-1/10-C ($\Delta = 36.4\ \eta_k$), C-1/10-M ($\Delta = 18.2\ \eta_k$) and C-1/10 ($\Delta = 9.1\ \eta_k$), where the estimated average viscosity ratios are 0.14, 0.04, 0.02, respectively. In these cases, the highest viscosity ratios with the values of 2.72 (C.1-10-C), 1.3 (C.1-10-M) and 0.59 (C.1-10) are found at the mixing layer near the nozzle.

As seen in Fig. 19, the calculated viscosity ratios even in the coarse case C-1/10-C never reach the critical quantity of five according to Celik et al.[92], or 20 according to Pettit et al. [75]. The simulations in this work can therefore be considered to be of good quality, however not fully resolved (DNS) despite of

over 560 Million cells.

5. Conclusion

This work investigated an impulsively started jet by highly resolved large eddy simulation (LES), in which the acquired data are validated by the experimental data from Soulopoulos et al. [45]. Our initial investigation of the experimental data showed that the resolution of the experiments was lower than the resolution of the simulations; hence the numerical validation yielded considerable differences. We consider that the laser beam profile and the correction filters in the experiments decreased the resolution further.

The experimental jet did not indicate a potential core, whereas our simulation showed one, consistent with the literature. This provided evidence for the conclusion of Soulopoulos et al. [88] that the entrained air was mixed inside the nozzle. Filtering and post-processing the numerical and experimental data fields gave an acceptable agreement with the experiments.

The initial injection and the development phase of the jet were studied by comparing our data qualitatively and statistically at different times. The predicted penetration length and the jet tip velocity were in a good agreement with the theoretical and experimental data. Some important starting-jet flow dynamics properties, such as the vortex ring, jet break-up and axisymmetric column structure were expectedly observed.

The present study shows that various physical parameters and the boundary conditions affect the results in a way that cannot be easily tested experimentally, such as the ramp-up (ramp-down) duration and function, inlet velocity profile, the turbulent length scale and intensity, and the inlet mixture ratio. Hence, we conducted a parameter study to identify the effect and likely parameter values, generating a better idea of the physics involved.

After fine-tuning of the boundary conditions, we achieved penetration lengths very similar to those from the experiments. However, the width of the jet in the simulation was slightly narrower than that from the experiment. The resolution achieved in the experiments yielded a thicker mixing layer than the analytically calculated one, which should explain the larger plume area/volume of the experimental jet compared to the numerical one with much higher resolution. It was also observed that a similar filter applied to the mixture fraction field of the simulation yielded a better agreement with the experiment.

Finally, we calculated the smallest resolved scales to enlighten the difference between the numerical and the experimental resolution. The simulations resolved flow scales smaller than the experiments by a factor of two. The quantitative results from the comparison showed that the SDR values of the simulation were higher than the ones measured by a factor of ten, however these high SDR were found on similar locations for both experiments and simulations.

It was observed that the PDFs of the conditional SDR are in good agreement with the same Gaussian

distribution, as in the Literature. The resolution of the data, the SDR calculated from the two or three dimensional gradient, the employed viscosity to calculate the SDR and the time of the evolving jet did not influence the shape of the PDFs. Also, the PDFs preserve their shape for different realizations.

The statistical analysis of the conditional SDR yielded these findings: In very early phases, the highest SDR values were found in the mixture fraction region of $0.4 - 0.6$ located on the mixing layers of the plume. The SDR decreased over time mostly in the mixture fraction range of $0.6 - 0.8$, mainly in the 'wound' up mixing layers inside the vortex ring. It was seen that the cluster of low SDR values in the vortex ring shifted from high mixture fraction values ($\tilde{f} = 0.6 - 0.8$) to lower values ($\tilde{f} = 0.5 - 0.7$), and the SDR values further decreased. This was due to the mixing process in the vortex ring, which completed rapidly until the entrained air was totally mixed.

It should however be noted that some of the findings from the simulations could not be validated due to unavailability of the additional experimental data, and we would like to encourage experimentalists to further investigate this interesting flow.

Acknowledgments

The authors gratefully acknowledge the financial support by the state North-Rhine-Westphalia, Germany. Our appreciation goes to Dr. Soulopoulos and Profs. Taylor and Hardalupas for their support. We also thank the University of Duisburg-Essen and Center for Computational Sciences and Simulation (CCSS) for providing the supercomputer magnitUDE (DFG grant INST 20876/209-1 FUGG) at the Zentrum für Informations- und Mediendienste (ZIM).

[1] T. Takagi, T. Okamoto, A. Ohtani, M. Komiyama, Measurements of velocity and concentration in transient jets by LDV and Rayleigh scattering, JSME International Journal 31 (1) (1988) 119–126.

[2] N. Atassi, J. Boree, G. Charnay, Transient behavior of an axisymmetric turbulent jet, Applied Scientific Research 51 (1993) 137–142.

[3] J. Turner, The starting plume in neutral surroundings., Journal of Fluid Mechanics 13 (1962) 356–368.

[4] F. Lahbabi, J. Boree, H. Nuglisch, G. Charnay, Analysis of starting and steady turbulent jets by image processing techniques, ASME 173 (1993) 315–321.

[5] I. Iglesias, M. Vera, A. L. Sanchez, Simulations of starting gas jets at low Mach numbers, Physics of Fluids 17 (038105) (2005) 1–4.

[6] K. Shariff, A. Leonard, Vortex rings, Annual Review of Fluid Mechanics 24 (1992) 235–279.

[7] N. Didden, On the formation of vortex rings: rolling-up and production of circulation, Zeitschrift fuer angewandte Mathematik und Physik 30 (1974) 101–116.

[8] M. Gharib, E. Rambod, K. Shariff, A universal time scale for vortex ring formation, Journal of Fluid Mechanics 360 (1998) 121–140.

[9] P. O. Witze, The impulsively started incompressible turbulent jet, SAND80-8167.

[10] P. O. Witze, Hot-film anemometer measurements in a starting turbulent jet, AIAA 21 (2) (1982) 308–309.

[11] A. Joshi, W. Schreiber, An experimental examination of an impulsively started incompressible turbulent jet, Experiments in Fluids 40 (2006) 156–160.

[12] H. Johari, Q. Zhangand, M. J. Rose, S. M. Bourque, Impulsively started turbulent jets, American Institute of Aeronautics and Astronautics 35 (4) (1997) 657–662.

[13] H. Johari, R. Paduano, Dilution and mixing in an unsteady jet, American Institute of Aeronautics and Astronautics 44 (11) (1997) 2719–2725.

[14] K. Bremhorst, H. Harch, The mechanism of jet entrainment, American Institute of Aeronautics and Astronautics 16 (10) (1978) 1104–1106.

[15] G. P. Hill, P. Ouellette, Transient turbulent gaseous fuel jets for diesel engines, Journal of Fluids Engineering 121 (1) (1999) 93–101.

[16] M. Nitsche, R. Krasny, A numerical study of vortex ring formation at the edge of a circular tube, Journal of Fluid Mechanics 276 (1994) 139–161.

[17] R. S. Heeg, N. Riley, Simulation of the formation of an axisymmetric vortex ring, Journal of Fluid Mechanics 339 (1997) 199–211.

[18] J. Janicka, W. Kollmann, Prediction model for the PDF of turbulent temperature fluctuations in a heated round jet, Proceeding of the Second Symposium On Turbulent Shear Flows 1 (1979) 7–11.

[19] M. Rosenfeld, E. Rambod, M. Gharib, Circulation and formation number of laminar vortex rings, Journal of Fluid Mechanics 376 (1998) 297–318.

[20] W. Zhao, S. H. Frankel, L. G. Mongeau, Effects of trailing jet instability on vortex ring formation, Physics of Fluids 12 (3) (2000) 589–596.

[21] H. B. Toda, O. Cabrit, K. Truffin, G. Bruneaux, F. Nicoud, Assessment of subgrid-scale models with a large-eddy simulation-dedicated experimental database: The pulsatile impinging jet in turbulent cross-flow, Physics of Fluids 26 (7) (2014) 075108.

[22] A. R. Masri, R. Cao, S. B. Pope, G. M. Goldin, PDF calculations of turbulent lifted flames of H2/N2 fuel issuing into a vitiated co-flow, Combustion Theory and Modelling 8 (2004) 1–22.

[23] M. J. Papageorge, C. M. Arndt, F. Fuest, W. Meier, J. A. Sutton, High-speed mixture fraction and temperature imaging of pulsed and turbulent fuel jets auto-igniting in high-temperature and vitiated co-flows, Experiments in Fluids 55 (1763) (2014) 1–20.

[24] C. M. Arndt, R. Schiessl, J. D. Gounder, W. Meier, M. Aigner, Flame stabilization and auto-ignition of pulsed methane jets in a hot coflow: Influence of temperature, Proceedings of the Combustion Institute 34 (2012) 1483–1490.

[25] H. Knabben, W. Kollmann, C. G. Stojanoff, Statistische untersuchung einer turbulenten, reagierenden stroemung, Archiwum Procesow Spalania 5 (1974) 295–310.

[26] S. M. Kato, B. C. Groenewegen, R. E. Breidenthal, Turbulent mixing in nonsteady jets, American Institute of Aeronautics and Astronautics 25 (1) (1987) 165–168.

[27] K. B. Southerland, J. R. Porter, W. J. A. Dahm, K. A. Buch, An experimental study of the molecular mixing process in an axisymmetric laminar vortex ring, Physics of Fluids 3 (5) (1991) 1385–1392.

[28] H. Viets, Flip-flop jet nozzle, American Institute of Aeronautics and Astronautics 13 (10) (1975) 1375–1379.

[29] K. Bremhorst, H. Harch, Near field velocity measurements in a fully pulsed subsonic air jet, Turbulent Shear Flows 1 (1979) 37–54.

[30] K. Bremhorst, R. D. Watson, Velocity field and entrainment of a pulsed core jet, Journal of Fluids Engineering 103 (4) (1981) 605–608.

[31] A. E. Sreenivasan, On local isotropy of passive scalar in turbulent shear flows, Proceedings: Mathematical and Physical Sciences 434 (1890) (1991) 165–182.

[32] Z. Warhaft, Passive scalar in turbulent flows, Annual Review of Fluid Mechanics 32 (1) (2000) 203–240.

[33] P. Dimotakis, Turbulent mixing, Annual Review of Fluid Mechanics 37 (2005) 329–356.

[34] R. W. Dibble, W. Kollmann, R. W. Schefer, Measurements and predictions of scalar dissipation in turbulent jet flames, Symposium (International) on Combustion 20 (1) (1985) 345–352.

[35] C. Tong., Z. Warhaft, Scalar dispersion and mixing in a jet, Journal of Fluid Mechanics 292 (1995) 1–38.

[36] D. Dowling, The estimated scalar dissipation in gas-phase turbulent jets, Physics of Fluids 3 (9) (1991) 2229–2246.

[37] K. Buch, W. Dahm, Experimental study of the fine scale structure of conserved scalar mixing in turbulent shear flows, Journal of Fluid Mechanics 317 (1996) 21–71, part 1.

[38] K. Buch, W. Dahm, Experimental study of the fine scale structure of conserved scalar mixing in turbulent shear flows, Journal of Fluid Mechanics 364 (1998) 1–29, part 2.

[39] L. K. Su, N. Clemens, The structure of fine-scale scalar mixing in gas-phase planar turbulent jets, Journal of Fluid Mechanics 488 (2003) 1–29.

[40] M. Namazian, R. W. Schefer, J. Kelly, Scalar dissipation measurements in the developing region of a jet, Combustion and Flame 74 (2) (1988) 147–160.

[41] R. Schefer, A. Kerstein, M. Namazian, J. Kelly, Role of large-scale structure in a non-reacting turbulent CH4 jet., Physics of Fluids 6 (2) (1994) 652–661.

[42] R. A. Antonia, J. Mi, Temperature dissipation in a turbulent round jet, Journal of Fluid Mechanics 28 (4) (1993) 1048–1054.

[43] V. Eswaran, S. B. Pope, Direct numerical simulations of the turbulent mixing of a passive scalar, Physics of Fluids 31 (506).

[44] J. Mi, R. A. Antonia, F. Anselmet, Joint statistics between temperature and its dissipation rate components in a round jet, Physics of Fluids 7 (7) (1995) 1665–1673.

[45] N. Soulopoulos, Y. Hardalupas, A. M. K. P. Taylor, Scalar dissipation rate measurements in a starting jet, Experiments in Fluids 55 (1685) (2014) 1–20, springer.

[46] N. Soulopoulos, Y. Hardalupas, A. M. K. P. Taylor, Mixing and scalar dissipation rate statistics in a starting gas jet, Physics of Fluids 27 (12) (2015) 125103.

[47] G. Wang, A. N. Karpetis, R. S. Barlow, Dissipation length scales in turbulent nonpremixed jet flames, Combustion and Flame 148 (2007) 62–75.

[48] T. D. Dunstan, Y. Minamoto, N. Chakraborty, N. Swaminathan, Scalar dissipation rate modelling for Large Eddy Simulation of turbulent premixed flames, Proceedings of the Combustion Institute 34 (2013) 1193–1201.

[49] T. Ma, Y. Gao, A. M. Kempf, N. Chakraborty, Validation and implementation of algebraic LES modelling of Scalar Dissipation Rate for reaction rate closure in turbulent premixed combustion, Combustion and Flame 161 (12) (2014) 3134–3153.

[50] H. Pitsch, H. Steiner, Scalar mixing and dissipation rate in large-eddy ssimulation of non-premixed turbulent combustion, Proceedings of the Combustion Institute 28 (2000) 41–49.

[51] J. M. McDonough, Introductory Lectures on Turbulence, Departments of Mechanical Engineering and Mathematics University of Kentucky, 2004.

[52] A. M. Kempf, F. Flemming, J. Janicka, Investigation of length-scales, scalar dissipation and flame orientation in a piloted diffusion flame by LES, Proceedings of the Combustion Institute 30 (2005) 557–565.

[53] H. Wang, M. Juddoo, S. H. Starner, A. R. Masri, S. B. Pope, A novel transient turbulent jet flame for studying turbulent combustion, Proceedings of the Combustion Institute 34 (2013) 1251–1259.

[54] J. P. H. Sanders, I. Gökalp, Scalar dissipation rate modelling in variable density turbulent axisymmetric jets and diffusion flames, Physics of Fluids 10 (4) (1997) 938–948.

[55] A. Yoshizawa, Statistical modelling of passive-scalar diffusion in turbulent shear flows, Journal of Fluid Mechanics 195 (1988) 541.

[56] K. N. C. Bray, Turbulent flows with premixed reactants, Springer-Verlag, New York (1980) 115–183.

[57] A. Y. Klimenko, R. W. Bilger, Conditional moment closure for turbulent combustion, Progress in Energy and Combustion Science 25 (1999) 595–687.

[58] S. B. Pope, PDF methods for turbulent reactive flows, Progress in Energy and Combustion Science 11 (1985) 119–192.

[59] N. Peters, Laminar diffusion flamelet model in non-premixed combustion, Progress in Energy and Combustion Science (1984) 319.

[60] I. K. Ye, Investigation of the scalar variance and scalar dissipation rate in urans and les, Ph.D. thesis, University of Waterloo (2011).

[61] A. M. Kempf, A. Sadiki, J. Janicka, Prediction of finite chemistry effects using large-eddy simulation, Proceedings of the Combustion Institute 29 (2002) 1979–1985.

[62] R. W. Bilger, The structure of diffusion flames, Combustion Science and Technology 13 (1976) 155–170.

[63] D. Butz, Y. Gao, A. M. Kempf, N. Chakraborty, Large eddy simulations of a turbulent premixed swirl flame using an algebraic scalar dissipation rate closure, Combustion and Flame 162 (9) (2015) 3180–3196.

[64] T. Tanaka, J. Eaton, A correction method for measuring turbulent kinetic energy dissipation rate by PIV, Experiments in Fluids 42 (6) (2007) 893–902.

[65] T. Poinsot, D. Veynante, Theoretical and Numerical Combustion, 3rd Edition, Aquaprint, Bordeaux, France, 2001.

[66] G. K. Batchelor, I. D. Howells, A. A. Townsend, Small-scale variation of convected quantities like temperautre in turbulent fluid, Journal of Fluid MechanicsPart 2.

[67] R. W. Bilger, The structure of turbulent nonpremixed flames, Proceedings of the Combustion Institute 22 (1988) 475–488.

[68] J. Boussinesq, Essai sur la theorie des eaux courantes, Memoires presentes par divers savants a l'Academie des Sciences 23 (1) (1877) 1–680.

[69] J. Smagorinsky, General circulation experiments with the primitive equations, Monthly Weather Review 91 (3) (1963) 99 – 164.

[70] D. Lilly, Representation of small-scale turbulence in numerical simulation experiments, Proceedings of IBM Sci. Comp. Symp. on Environmental Sciences (1967) 195–210.

[71] F. Nicoud, H. B. Toda, O. Cabrit, S. Bose, J. Lee, Using singular values to build a subgrid-scale model for large eddy simulations, Physics of Fluids 23 (8).

[72] S. S. Girimaji, Y. Zhou, Analysis and modeling of subgrid scalar mixing using numerical data, Physics of Fluids 8 (1996) 1224–1236.

[73] D. Geyer, A. M. Kempf, A. Dreizler, J. Janicka, Scalar dissipation rates in isothermal and reactive turbulent opposed-jets: 1-D-Raman/Rayleigh experiments supported by LES, Proceedings of the Combustion Institute (2005) 681–689.

[74] O. T. Stein, B. Böhm, A. Dreizler, A. M. Kempf, Highly-resolved LES and PIV analysis of isothermal turbulent opposed jets for combustion applications, Turbulence and Combustion 87 (2-3) (2011) 425–447.

[75] M. W. A. Pettit, B. Coriton, A. Gomez, A. M. Kempf, Large-eddy simulation and experiments on non-premixed highly turbulent opposed jet flows, Proceedings of the Combustion Institute 33 (1) (2011) 1391–1399.

[76] A. M. Kempf, B. Geurts, J. C. Oefelein, Error analysis of large-eddy simulation of the turbulent non-premixed sydney bluff-body flame, Combustion and Flame 158 (2011) 2408–2419.

[77] M. Rieth, F. Proch, O. T. Stein, M. W. A. Pettit, A. M. Kempf, Comparison of the Sigma and Smagorinsky LES models for grid generated turbulence and a channel flow, Computers and Fluids 99 (2014) 172–181.

[78] T. Nguyen, F. Proch, I. Wlokas, A. M. Kempf, Large eddy simulation of an internal combustion engine using an efficient immersed boundary technique, Flow, Turbulence and Combustion (2015) 1–40.

[79] G. Zhou, Numerical simulations of physical discontinuities in single and multi-fuid fows for arbitrary mach numbers, Ph.D thesis, Chalmers University of Technology, Goteborg, Sweden (1995).

[80] M. M. Rai, P. Moin, Direct simulations of turbulent flow using finite difference schemes, Journal of Computational Physics 96 (15) (1991) 53.

[81] P. A. Davidson, Turbulence, An Introduction for Scientists and Engineers, 2nd Edition, Oxford University Press, 2004.

[82] H. Tennekes, J. Lumley, A First Course in Turbulence, The MIT Press, 1972.

[83] M. Klein, A digital filter based generation of inflow data for spatially developing direct or numerical or large eddy simulation, Journal of Computational Physics.

[84] A. M. Kempf, S. Wysocki, M. Pettit, An efficient and parallel low storage implementation of Klein's turbulence generator for LES and DNS, Computers and Fluids 60 (2012) 58–60.

[85] G. E. Cossali, A. Coghe, L. Araneo, Near field entrainment in an impulsively started turbulent gas jet, American Institute of Aeronautics and Astronautics 39 (6) (2001) 1113–1122.

[86] L. J. W. Graham, K. Bremhorst, Application of the k-e turbulence model to the simulation of a fully pulsed free air jet, Journal of Fluids Engineering 115 (1) (1993) 70–74.

[87] K. Bremhorst, T. J. Craft, B. E. Launder, Two-time-scale turbulence modelling of a fully-pulsed axisymmetric air jet, Journal of Fluids Engineering.

[88] D. N. Soulopoulos, Imperial College London, personal communication (06.05.2015).

[89] S. A. Kaiser, J. H. Frank, The effects of laser-sheet thickness on dissipation measurements in turbulent non-reacting jets and jet flames., Measurement Science and Technology 22 (4).

[90] J. A. Sutton, J. F. Driscoll, Measurements and statistics of mixture fraction and scalar dissipation rates in turbulent non-premixed jet flames, Combustion and Flame 160 (2013) 1767–1778.

[91] C. N. Markides, N. Chakraborty, Statistics of the scalar dissipation rate using direct numerical simulations and planar laser-induced fluorescence data, Chemical Engineering Science 90 (2013) 221–241.

[92] I. B. Celik, Z. N. Cehreli, I. Yavuz, Index of resolution quality for large eddy simulations, Journal of fluids engineering 127 (5) (2005) 949–958.

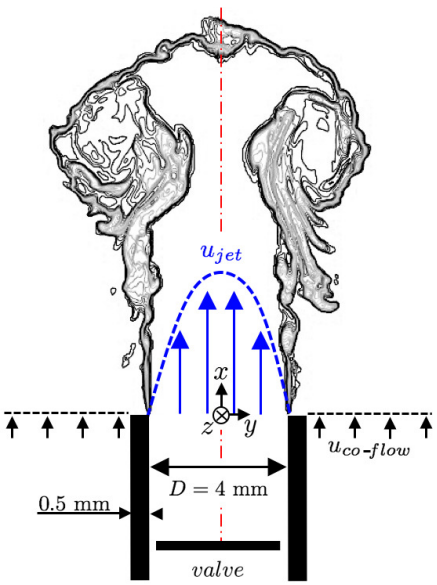

Figure 1: Flow configuration and the coordinate system [45].

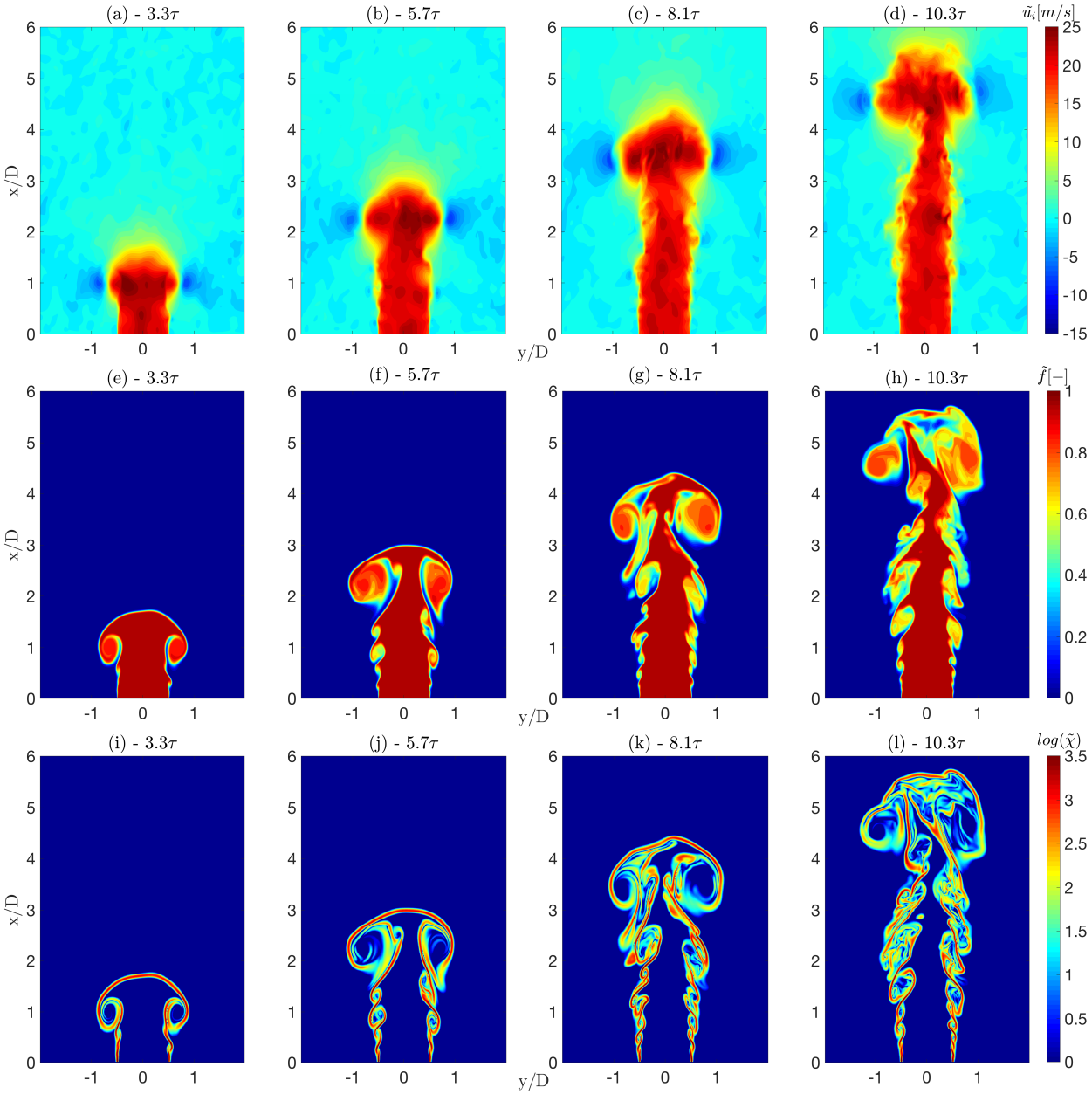

Figure 2: Time evolution in the central-plane at 3.3, 5.7, 8.1 and 10.3τ. The plots show the instantaneous axial velocity (a-d), the instantaneous mixture fraction (e-h), and the SDR (i-l) fields for C-1/10.

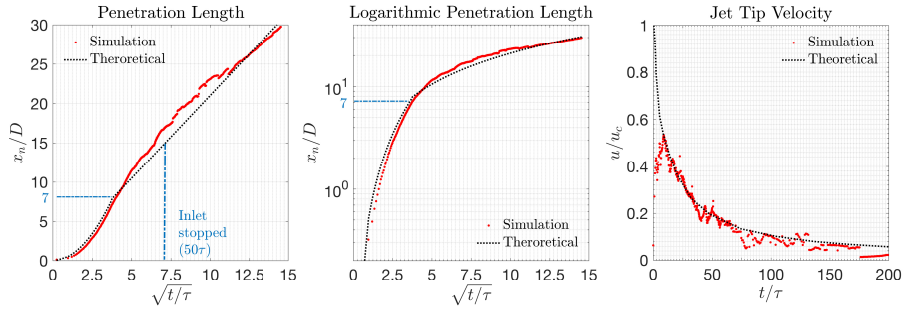

Figure 3: Jet penetration length as a function of the square root of non-dimensional time for C-1/10-C and the recorded jet tip velocities are shown alongside with the fitted theoretical solutions from Witze's work [11].

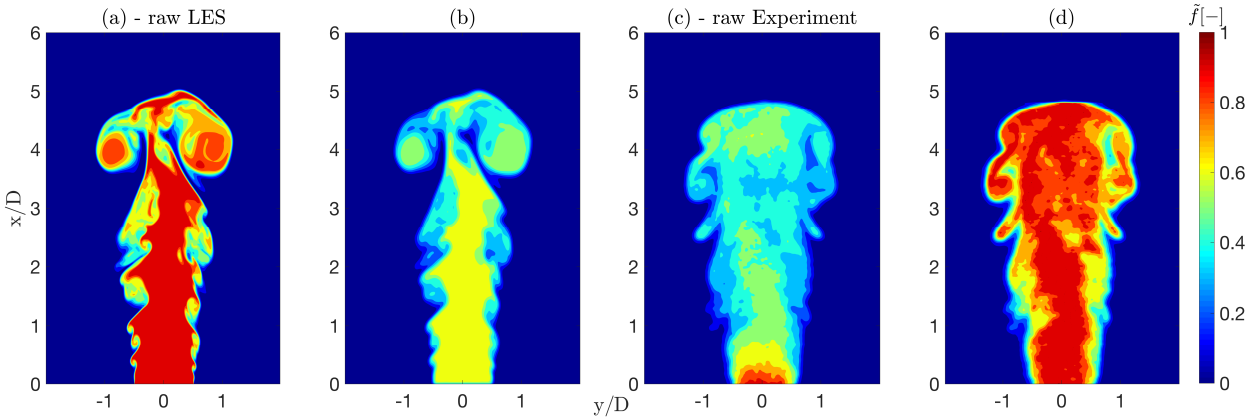

Figure 4: Instantaneous mixture fraction $\tilde{f}$ from raw LES (a), rescaled and filtered LES (b), experiment (c) and post-processed experimental (d) data at the time 9.65τ. The numerical data are taken from C-1/10 with 563 million cells.

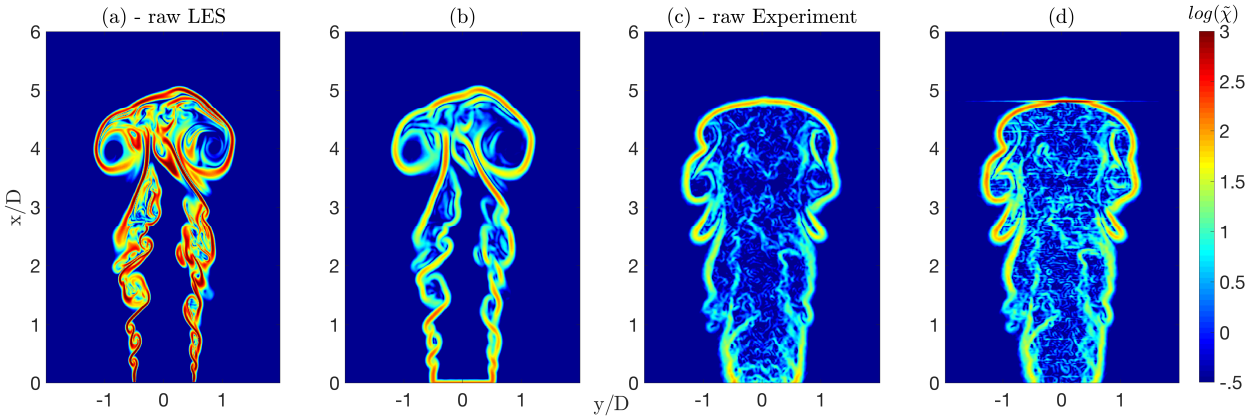

Figure 5: Instantaneous SDR χ from raw LES (a), rescaled and filtered LES (b), experiment (c) and post-processed experimental (d) data at the time 9.65τ. The numerical data are taken from C-1/10, 563 million cells. Except for (a), the SDR is calculated from the two dimensional gradient.

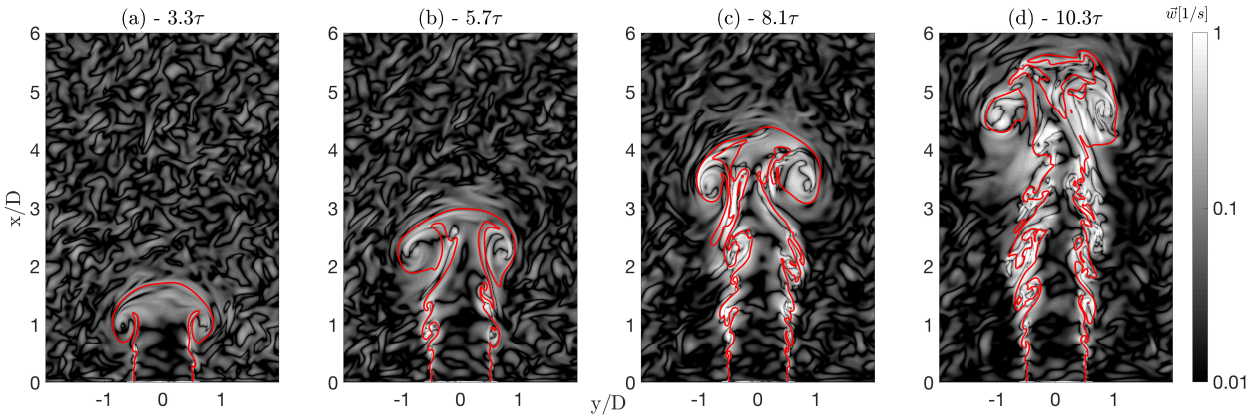

Figure 6: Vorticity in the central-plane at [3.3, 5.7, 8.1, 10.3τ] (C-1/10). The main mixing layer is highlighted by the red line.

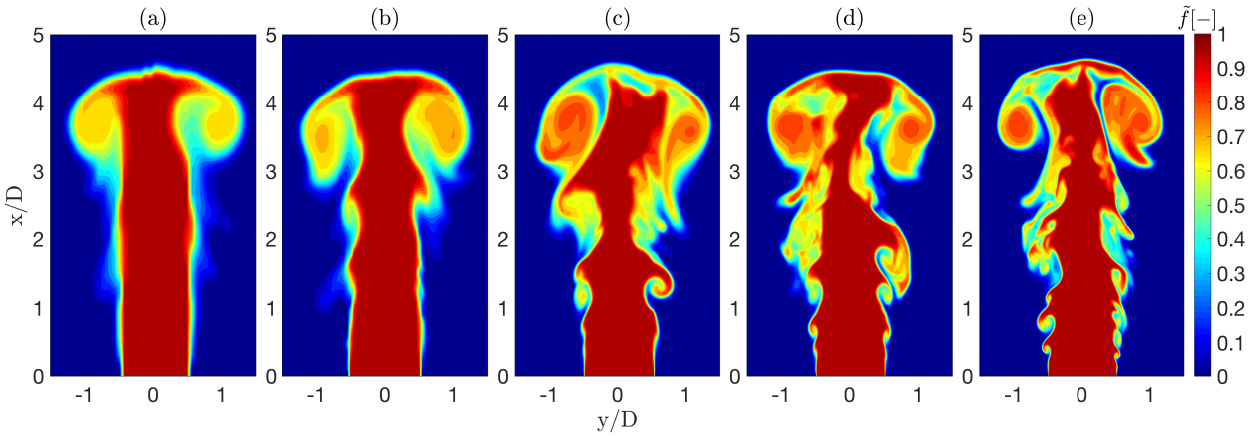

Figure 7: Mixture fraction at 9.65τ obtained on five different grids of the central-plane for C-2/3 (a), C-1/2 (b), C-1/4 (c), C-1/6 (d) and C-1/10 (e), respectively, as described in Table 1

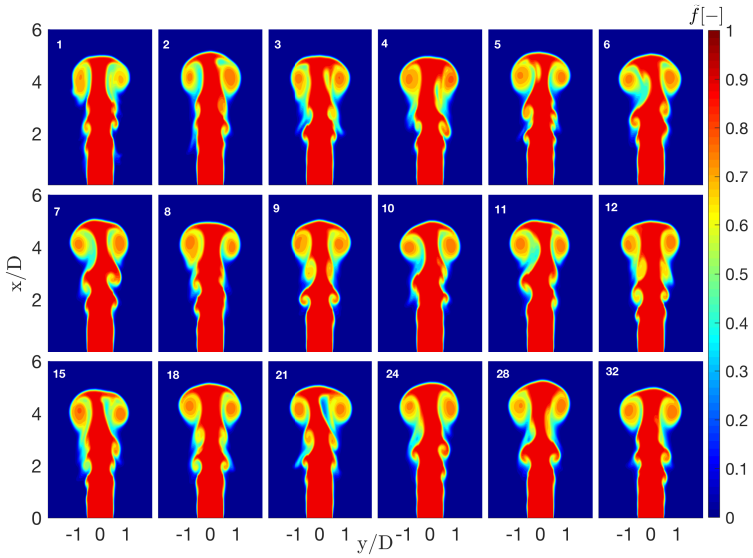

Figure 8: Different realisations of the impulsively started jet presented by raw instantaneous mixture fraction, each at SoI time of 9.65τ in the central-plane. The white number at top left of each plot shows the realisation number. The case parameters can be found in Table 1

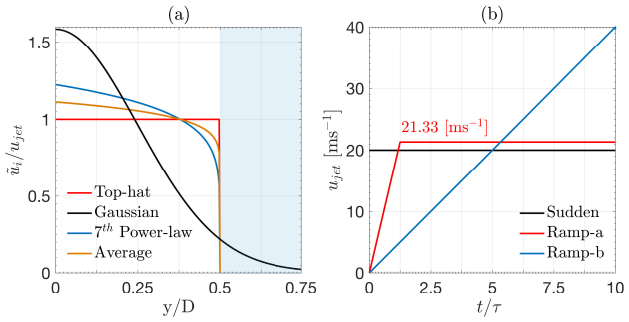

Figure 9: Normalised centreline velocity over the nozzle diameter (a) and centreline velocity over time (b) during ramp-up.

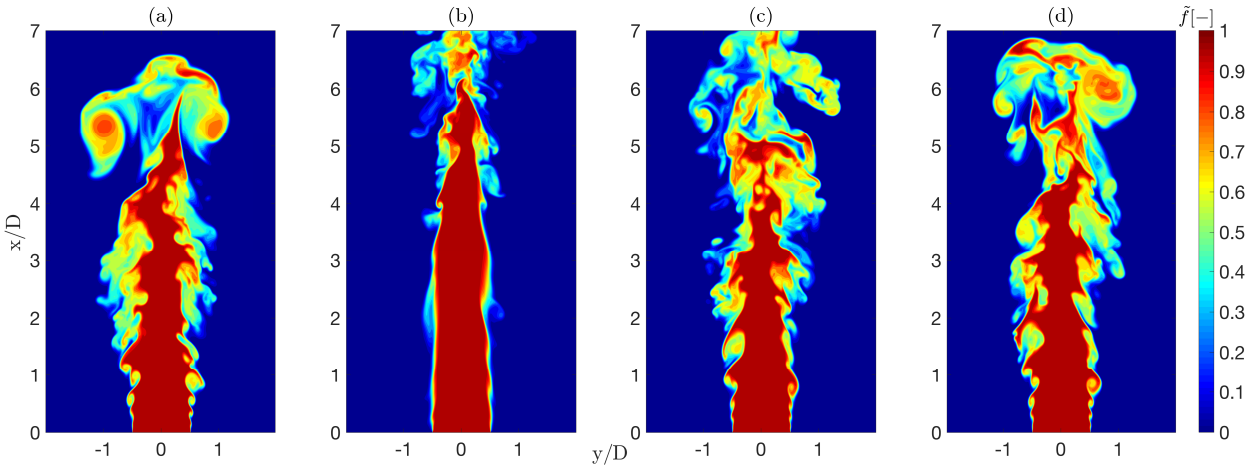

Figure 10: Instantaneous mixture fraction at 13.4τ for different inlet velocity profiles: Top-hat (a), Gaussian (b), 7^{th} power-law (c) and the average of the top-hat and the 7^{th} power law (d).

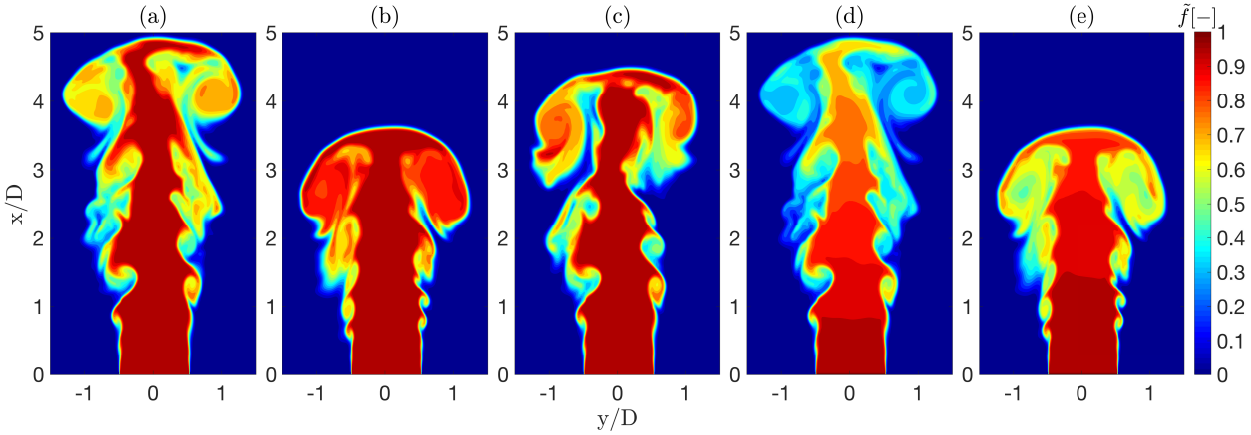

Figure 11: Instantaneous mixture fraction at 10τ. Suddenly started injection (a) is compared with the simulations that have the parameters; the inlet velocity (b), the turbulence intensity (c) and the mixture fraction (d) are linearly ramped with *Ramp-b* function. These are then compared with the simulation, where all of the parameters are jointly ramped (e) for further analysis. The study parameters are given in Table 2, *Study 4*.

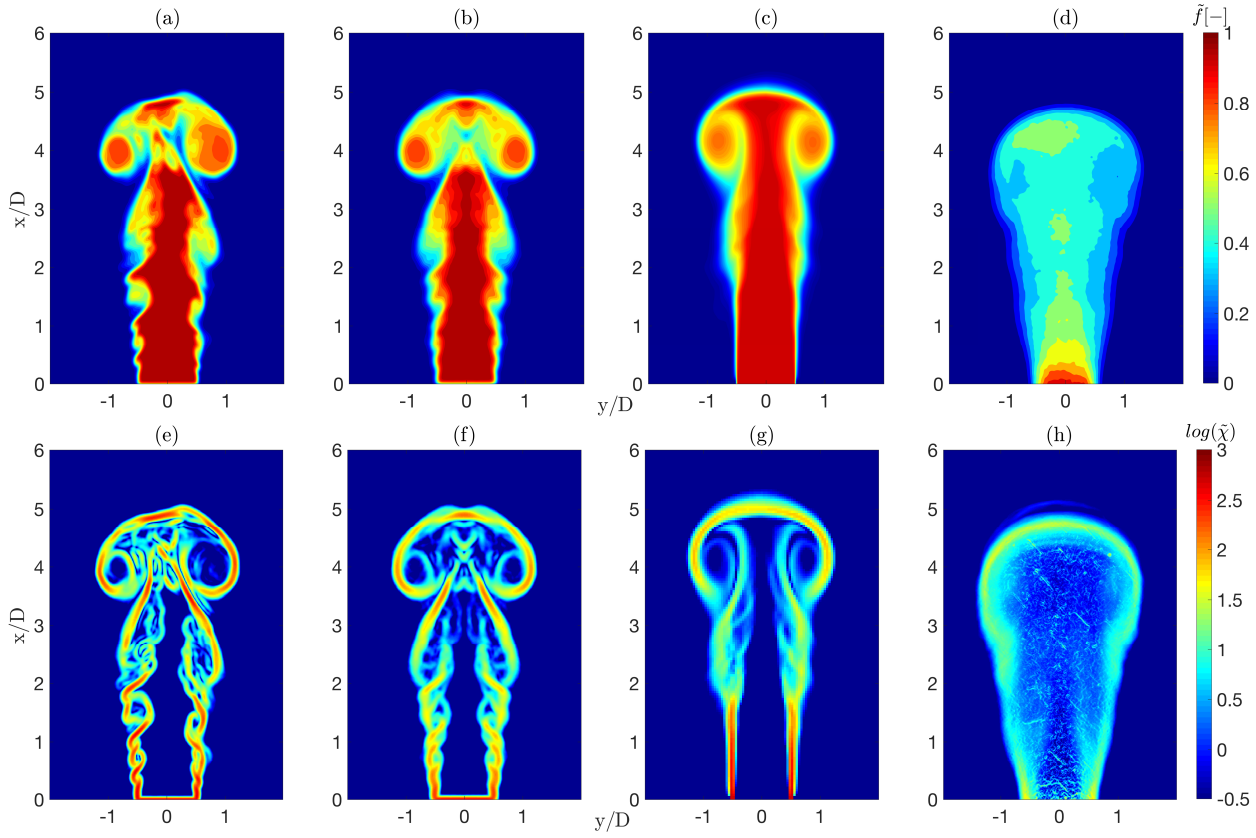

Figure 12: Top row presents averaged mixture fraction over two samples (a), four samples (b) from C-1/10 and 32 samples LES (c) from C-1/10-C, also the experimental plot averaged over 300 samples is shown (d). The bottom row shows the corresponding SDR from simulations (e-g) and experiment (h). Plot (c) presents the averaged mixture fraction over 32 consecutive injections obtained from C-1/10-C, which has lower resolution than C-1/10 (The SDR is calculated from the two gradient components).

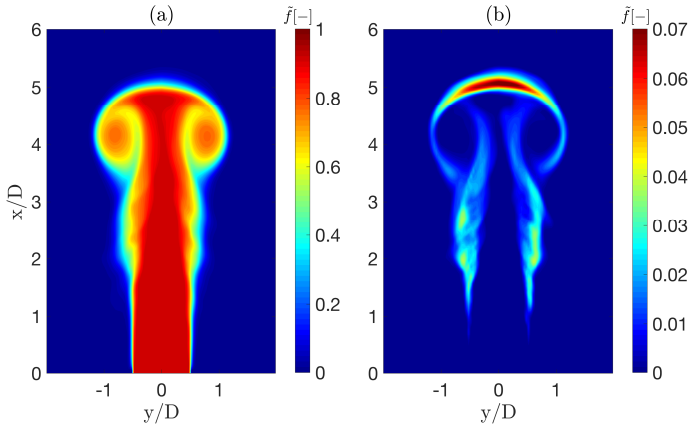

Figure 13: Averaged mixture fraction over 32 samples of C-1/10-C (a) with its RMS (b). The sampled data are taken for each SoI at 9.65τ.

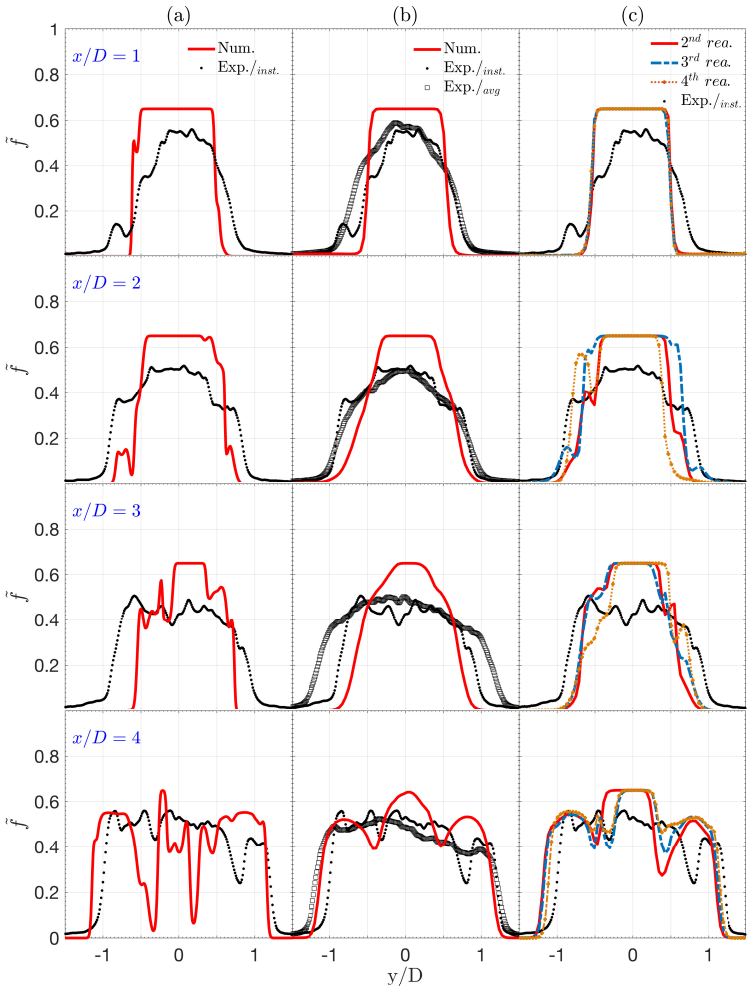

Figure 14: Mixture fraction radial profiles of calculated and rescaled instantaneous (a) and averaged over 32 injections (b) at 9.65τ. Plot a shows data from C-1/10, and plot b presents averaged data obtained from C-1/10-C. From the top row to the bottom, the data are shown for the axial distances of $x/D = 1, 2, 3, 4$. Three consecutive realisations (2-4) jet profiles (b) taken from C-1/10-C are shown as well. Black dots and circles represent the instantaneous and averaged (over 300 samples) experimental profiles, respectively.

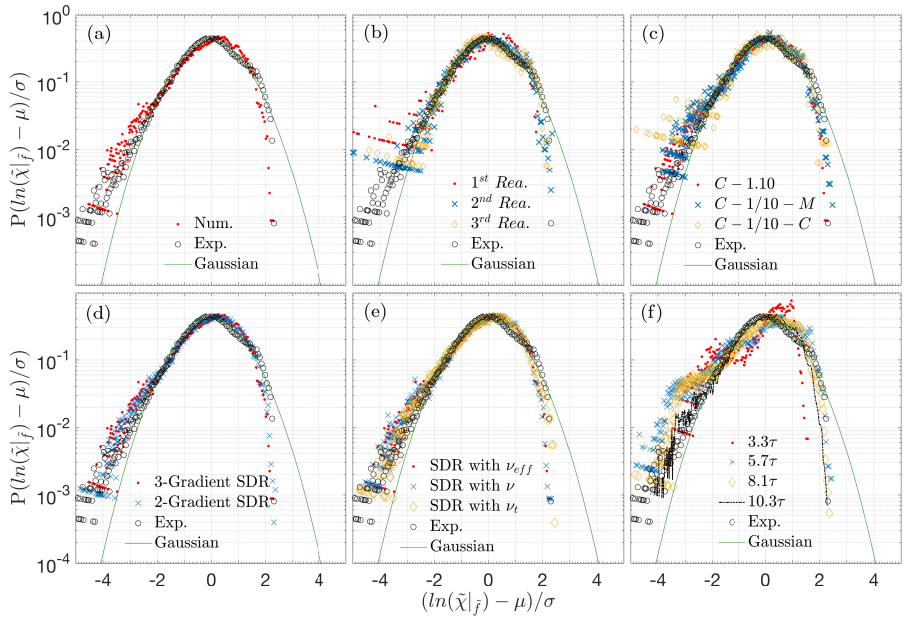

Figure 15: The PDFs of the normalized conditional logarithm of the SDR calculated from the instantaneous LES (C-1/10) and the raw experimental data taken in the central-plane at 9.65τ are shown in (a). PDFs of three consecutive injections from C-1/10-C are presented in (b), and (c) shows the PDFs from three different simulations with different grid sizes. The effect of the SDR that is calculated with two or three dimensional gradients (d), and with different viscosities (e) to the PDFs are illustrated. The PDFs of SDR's time evaluation is given in (f), where the data are taken from C-1/10 at times [3.3, 5.7, 8.1, 10.3τ]. The green line shows the Gaussian function, all SDR values are conditioned on $\tilde{f} > 0.05$.

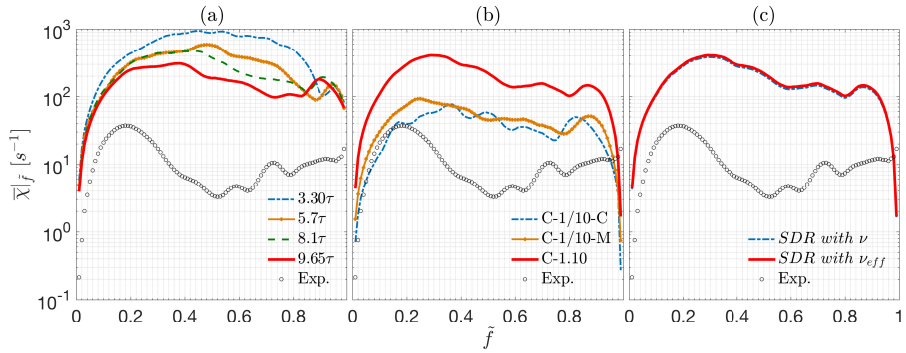

Figure 16: Time evolution (a) and grid dependency (b) of the conditional averages of SDR. For (a), the numerical data are taken at times 3.3, 5.7, 8.1 and 9.65τ from C-1/10, and experiments at 9.65τ. The conditional averages of SDR obtained from C-1/4, C-1/6 and C-1/10 are shown in (b). The SDR is conditioned on the mixture fraction $\tilde{f} > 0.01$. The contribution of the SDR sub-grid model is presented in (c). The conditional averages of SDR are given in log-normal scales.

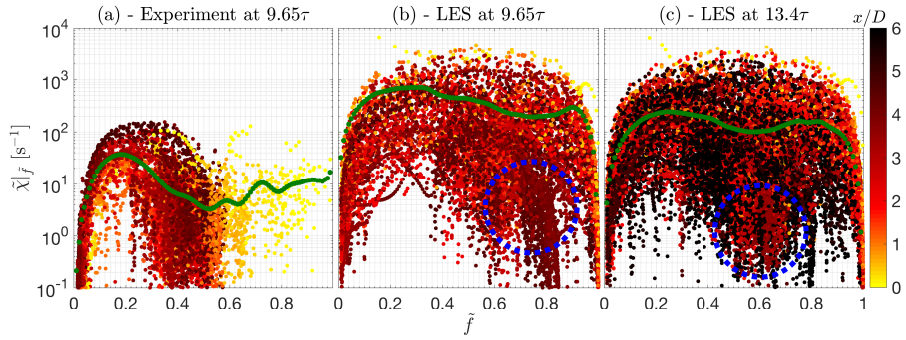

Figure 17: Scatter plots of the instantaneous conditional SDR over mixture fraction. The experiment is at 9.65τ (a) and the numerical data are taken from C-1/10 at times of 9.65τ (b) and 13.4τ (c). The color-map indicates the distance of the SDR values in axial direction. The SDR values are conditioned on $\tilde{f} > 0.01$. The green line indicates the averaged conditional distribution, and dashed blue circles emphasize the cluster of calculated low SDR located in the vortex core. The SDR-axis is given in log-scales.

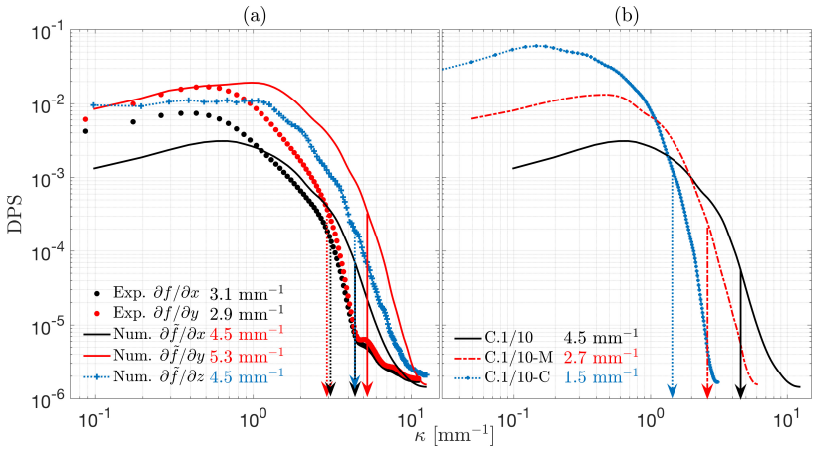

Figure 18: Calculated axial ($\partial \tilde{f}/\partial x$), radial ($\partial \tilde{f}/\partial y$) and circumferential ($\partial \tilde{f}/\partial z$) derivative spectra from C.1-10 (a) and radial spectra from three simulations with different filter sizes (b), compared to the experimental spectra marked with black dots. The DPS is estimated in the region of $x/D < 5$ and $-1.5 < y/D < 1.5$ and $z/D = 4$ at 9.65τ. The layer at $x/D = 4$ is chosen to estimate DPS for the circumferential direction. The wave numbers corresponding to 2% of the peak value are marked with arrows.

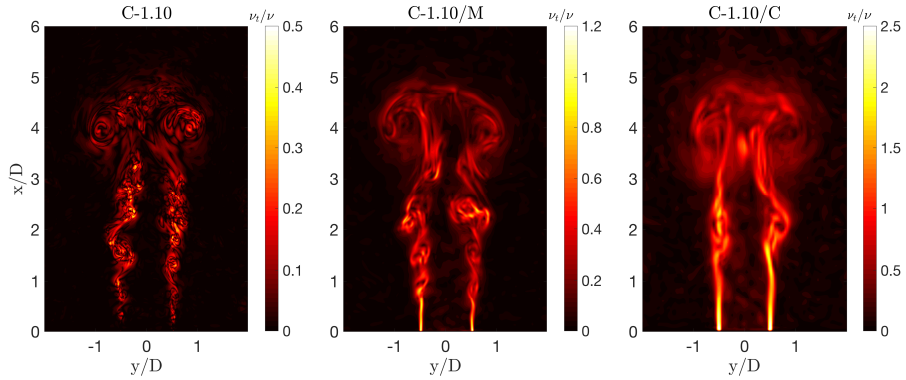

Figure 19: The estimated viscosity ratios for cases C-1/10-C, C-1/10-M and C-1/10 in the central-plane at 9.65τ